Assessing the chemical stability and cytotoxicity of electrodeposited magnetic mesoporous Fe–Pt films for biomedical applications

Albert Serrà [a,b,*], *David Limón* [b,c], *Natalia Díaz-Garrido,*[d] *Lluïsa Pérez-García* [b,c], *and Elvira Gómez* [a,b,*]

[a] Thin Films and Nanostructures Group, Department of Materials Science and Physical Chemistry, Facultat de Química, Universitat de Barcelona, Martí i Franquès, 1, E-08028, Barcelona, Catalonia, Spain.

[b] Institute of Nanoscience and Nanotechnology (IN^{2}UB), Universitat de Barcelona, Barcelona, Catalonia, Spain.

[c] Departament de Farmacologia, Toxicologia i Química Terapèutica, Facultat de Farmàcia i Ciències de l'Alimentació, Universitat de Barcelona, Avda. Joan XXIII 27-31, E-08028 Barcelona, Catalonia, Spain.

[d] Departament de Bioquímica i Fisiologia, Facultat de Farmàcia i Ciències de l'Alimentació, Universitat de Barcelona, Avda. Joan XXIII 27-31, E-08028 Barcelona, Catalonia, Spain.

Corresponding author: a.serra@ub.edu (A.S.); e.gomez@ub.edu (E.G.)

KEYWORDS: electrodeposition; Fe-Pt; mesoporous; chemical stability; cytotoxicity; biomedical applications

ABSTRACT:

The development of feasible micro/nanoplatforms for various biomedical applications requires holistic research that explores scalable synthesis and design pathways and imposes an interdisciplinary integration of materials science, physical, medical, chemical, and biological knowledge. Thanks to their unique characteristics (i.e., structure, large specific surface areas, tuneability, versatility, and integrity), mesoporous materials have emerged as important candidates for being part of micro/nanoplatforms for therapeutic, monitoring, and diagnostic applications. In this context, Fe-Pt mesoporous materials are excellent candidates to be part of biomedical micro/nanoplatforms thanks to their chemical nature, structure, and magnetic properties, which give them magnetic locomotion, high cargo capability of therapeutic agents inside the mesoporous cavity as well as large surface area for surface functionalization. However, the chemical stability in biological media and the cytotoxicity of Fe-Pt mesoporous material (without considering the effects of architecture and shape) are pivotal elements that determine the suitability of these materials for biomedical applications. This work demonstrates: (i) the potential of electrochemical deposition, based on the use of block-copolymer micellar solutions as electrochemical media, as an easy, inexpensive, and scalable strategy to synthesize mesoporous Fe-Pt components with tunable chemical composition, porosity, magnetism, and shape (in this case films but other architectures like nanowires can be easily fabricated by using simultaneously hard templates); (ii) the excellent corrosion stability, which is comparable to bulk

Au, and minimal chemical dissolution in biological media after 160 h of immersion (~0.88 % of Fe and ~0.0019 % of Pt), which confirms the robustness of Fe-Pt); (iii) negligible cytotoxicity on HaCaT cells (human immortalized keratinocytes), which reinforces the biocompatibility of Fe-Pt mesoporous structures. Also, the presence of Fe-Pt mesoporous films seems to induce a slight increase in cell viability. These results confirm the biocompatibility of Fe-Pt mesoporous films, making them suitable for biomedical applications.

TOC:

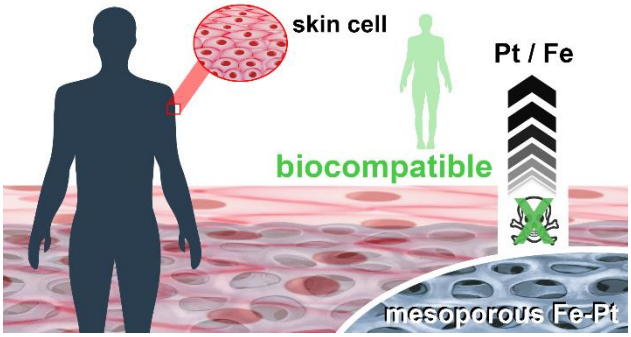

Introduction

Designing and fabricating new micro- and nanostructures for various applications in biomedicine and health science rank among the most exciting challenges in research today [1–4]. Overcoming such challenges in the field, however, requires the combined effort of scientists in diverse disciplines to select and prepare new materials, modify and incorporate them with new properties, and develop the means to control and track their actuation in real applications (e.g., the human body) or biological science [1,2,5]. Studying the viability of the nanostructures involved for applications in health medicine is another necessary undertaking. All of those challenges

have to be approached in interrelated ways to assure their applicability in real or near-future situations [1–4,6].

To date, many micro- and nanostructures have been developed that combine different materials in the same structure in order to extend their applicability and broaden their scope of operations. Combining materials with biological components can especially support the fabrication of hybrid micro- and nanostructures with enhanced biocompatibility and broader applicability [3,7–10].

To succeed in various biomedical applications, particularly in real in vivo biomedical applications, such materials need to satisfy certain prerequisites, including biocompatibility and precise real-time control dynamics. The driving force for controlling their movement could be supplied by external stimuli such as magnetic, electric, ultrasound, or light irradiation [11–14]. Among the various strategies available to facilitate motion control, magnetic steering perhaps shows the most promise. Alternatively, after being internalized in cells, the micro and nanostructures can be activated via the magnetic field, which provides another method of manipulating cells at the subcellular level [12–16].

Different physical, chemical, and electrochemical techniques have been employed in fabricating micro- and nanostructures [14,17,18]. Electrochemistry, although an ancient field of knowledge, has become of paramount importance in the synthesis of micro- and nanostructures by offering simple low-cost set-ups under mild conditions of operation [11,19–21]. Such setups rely upon electrodeposition, a complex heterogeneous process that occurs at the electrode-solution interface, in which electroactive species in solution coat a conductive substrate with the amount of deposited material controlled by the charge applied [22]. The type and concentration of the

components of the solution, as well as the applied potential or current, are critical to controlling the morphology and coating rate of the deposited metal [11,20,23].

For suitable deposits loaded with active therapeutic components as carriers, both the materials and superficial geometry are critical. Drug delivery platforms, for example, benefit from micro- and nanostructures able to accommodate high cargo-loading capabilities that can support adequate doses for drug release [24–27]. Today, using metallic substrates as carriers need highly effective surfaces that maximize the area exposed and thus the convenience of the application. Given that dynamic, structures with hollow interiors have attracted considerable interest owing to their large specific area and low density [24,25,28,29].

Mesoporous materials have recently made significant contributions to enhancing surface-to-area-to-volume ratios as innovative, sophisticated materials that accommodate a soft-template process, micelle-assisted electrodeposition, that is not only essential but also simple to prepare [30–34]. Micelle-assisted electrodeposition involves new cooperative, synergetic means of synthetizing mesoporous nanomaterials in single step electrochemical methods [32,35,36]. In those methods, micelles generated in the bath contribute to homogenizing the porous distribution during their growth, thereby allowing greater, more homogeneous distribution of porous in the material prepared. The presence of a block copolymer such as Pluronic 123 in the aqueous bath has previously been demonstrated to be a soft inductive tool for forming mesoporous structures as effective pore inductors [36–40].

For a carrier material in biomedical applications, one candidate is Fe–Pt mesoporous alloy, a magnetic material expecting the necessary low toxicity and chemical integrity for health-related applications [41–47]. Interest in mesoporous systems stems from their potential use as

pharmaceutical carriers that can help to overcome problems posed by the drug's specific positioning [6,48]. In this work, Pluronic 123 was selected as a porogen agent for Fe–Pt mesoporous materials, and to enhance the iron content in the deposits, the bath was optimized by enriching the concentration of Fe(II) [40]. Given the effect of iron's presence on the electroactive bath, namely as a handicap for the bath's stability because it tends to form oxo- hydroxo species, the bath was performed in acidic medium. Reactivity to the hydrogen reaction was minimized considering the compromise between the solution's chemical stability and the process's efficiency [40,42].

Using advanced techniques, the synthetized materials were analyzed to confirm the formation of Fe–Pt, its chemical composition and surface morphology, as well as any exhibition of magnetism. By tuning experimental parameters such as the concentration of the electroactive species and the applied potential, different kinds of deposits were prepared. As a potential carrier, the material's long-term chemical stability was examined both in a natural biological environment and under electrical stimulation. As a concept probe to assess the suitability of this material for biomedical applications, its cytotoxicity was evaluated in HaCaT cells (human immortalized keratinocytes), which were chosen as a model epithelial cell line for being widely used for studying the biocompatibility of materials[49–52] due to their high capacity to proliferate and differentiate *in vitro*,[49] and their ability to form biofilms on surfaces.[49,52]

Experimental Section

Electrodeposition and characterization of Fe–Pt mesoporous films

The mesoporous Fe–Pt films were potentiostatically electrodeposited using a triblock copolymer micellar solution. The micellar-based electrolyte contained 3 mM of Na_2PtCl_6 (Alfa Aesar), 7.2 mM of $FeCl_2$ (VWR), and 5 g L^{-1} of Pluronic P-123 triblock copolymer (Sigma Aldrich). The pH of the electrolyte was adjusted to 2.1 and 3.0 using 1 M of HCl or NaOH, and all of the solutions were prepared with MilliQ water (Millipore) with a resistivity of 18.2 MΩ cm (25 °C).

Electrochemical characterization and deposition were performed in a three-electrode cell (20 mL) connected to an Autolab PGSTAT30 potentiostat–galvanostat (Metrohm Autolab BV). Si/ Ti (15 nm)/Au (100 nm) substrates of 0.2 cm^2, a Pt spiral, and Ag|AgCl|KCl (3 M) were used as working, counter, and reference electrodes, respectively. The electrolyte was de-aerated with argon gas for 10 min before and between each experiment, with the working temperature fixed at 25.0 ± 0.1 °C. After electrodeposition, the Fe–Pt mesoporous films were washed with acidic water (pH = 2.4) and rinsed with MilliQ water in order to remove the deposited polymers.

Prior to the characterization of materials, the Fe–Pt deposits were subjected to 100 W of O_2 plasma for 45 min in order to remove traces of the triblock copolymer. Field-emission scanning electron microscopy (FE-SEM, JSM-7100), equipped with an energy-dispersive X-ray spectroscopy detector, was used to analyze the morphology and elemental composition of the Fe–Pt mesoporous films. The specific surface area was evaluated based on the Brunauer–Emmett–Teller (BET) method from N_2 adsorption-desorption isotherms at 77 K using a Micrometrics Tristar-II. The elemental composition was also confirmed by X-ray fluorescence analysis (Fischerscope X-ray XDV-SDD) and ICP-OES analysis (Perkin Elmer 4300DV) after the digestion of deposits in aqua regia. X-ray diffraction (XRD) analysis (Bruker D8 Discovery diffractometer) in the Bragg–Brentano configuration with Cu K_α radiation was performed to study the films' crystallinity. X-ray photoelectron spectroscopy (XPS) analysis (PHI ESCA-5500

Multitechnique system) using monochromatic Al K_α radiation (i.e., Al K_α line of 1,486.6 eV energy and 350 W) as a source of excitation was applied to investigate the chemical state of the deposited metals. All binding energies (BEs) were calibrated using C 1s peak (BE = 284.8 eV).

Chemical and Electrochemical stability of Fe–Pt mesoporous films

For determining the chemical stability of Fe-Pt films in biological media, Si/Ti/Au substrates with Fe-Pt films deposited at -900, -1,000, and -1,100 mV were immersed in Dulbecco's modified Eagle's culture medium supplemented with 10% fetal bovine serum (FBS) and 10 mg mL^{-1} penicillin and streptomycin and 25 µg mL^{-1} of amphotericin B (DMEM).

Corrosion tests were performed in a three-electrode cell (100 mL) connected to an Autolab PGSTAT30 potentiostat–galvanostat using DMEM as the electrolyte, after which the steady-state potentials (E_{ss}) were determined with a polarization scan. Next, a linear potentiodynamic sweep from E_{ss} + 300 mV to -300 mV at 0.1 mV s^{-1} was performed to determine the corrosion potential (E_{corr}) and current density corrosion (j_{corr}) of the mesoporous Fe–Pt films. The mesoporous Fe–Pt films were subsequently immersed in DMEM for 24, 48, and 160 h at 37 °C in order to investigate their chemical stability in biological media. Following immersion, the concentration of Pt and Fe species on the supernatant was examined in ICP-OES analysis (Perkin Elmer 4300DV).

Mechanical stability of Fe–Pt mesoporous films

The reduced Young's modulus (Er) and hardness (H) of the Fe–Pt mesoporous films were determined with a Nanoindenter® XP system (Agilent Technologies) and a Berkovich diamond tip as part of the continuous stiffness measurement (CSM) method, which allowed the

continuous measurement of stiffness and applied load as a function of penetration depth. On each sample, 20 indentations were made, and mechanical properties were calculated as functions of penetration depth using the Oliver–Pharr approach. Penetration depth was limited to less than 10% of the film's thickness, given the widely reported negligible influence of the substrate at that penetration depth[53].

Cytotoxicity of Fe–Pt mesoporous films

The cytotoxicity of the biofilms was evaluated in HaCaT keratinocytes by means of a (3-(4, 5-dimethylthiazolyl-2)-2, 5-diphenyltetrazolium bromide) (MTT) assay. Cells were seeded in 48-well plates and were grown in DMEM (0.5 mL) at 37 ºC and 5% CO_2 to 80% confluency (~48 h). The medium was replaced for fresh one, and Si/Tui/Au substrates (0.25 cm^2) containing Fe-Pt films deposited at -900, -1,000, and -1,100 mV were immersed in each well. Cells were also incubated in the presence of Si/Ti/Au substrates without Fe-Pt, as well as without any substrate (untreated) as controls. Cells were incubated for 48 h at 37 ºC and 5% CO_2, after which the medium was replaced for a solution of MTT (0.5 mg mL^{-1}, 0.5 mL) in DMEM, and cells were further incubated for 2 h. The MTT solution was removed and DMSO (0.5 mL) was added to lyse cells and dissolve formazan crystals. The respective solutions were transferred to 96-well plates and the absorbance of each was measured at 561 nm in a Microplate Autoreader. All experiments were performed in triplicate. The cell viability was calculated respect to untreated cells and Kruskall-Wallis with Dunn's multiple comparison tests were performed using GraphPad Prism v.5.0 to determine significant differences ($P<0.05$) between samples.

Results and discussion

Electrodeposition and characterization of Fe–Pt mesoporous films

How the different components of polymeric micellar solution (i.e., pH, P-123, and electroactive species) affect electrodeposition onto Si/Ti/Au substrates was systematically investigated using cyclic voltammetry (CV), with the ionic strength of the electrochemical media fixed and adjusted with KCl. **Figure 1a** shows the CV of blank solutions of pH 2.1 (black line) and 3.0 (red line). A clear reduction in current signal, starting at approximately −0.50 V, appeared in the cathodic scan at pH 2.1, whereas an analogous but smaller reduction in signal commenced at more negative potentials (i.e., approx. −0.70 V) at pH 3.0. The inset in **Figure 1a** illustrates the voltamperometric response of the solution at a pH of 2.1 in stagnant (red) and stirred (black) conditions at a scan rate of 50 mV s^{-1} on the Si/Ti/Au substrates. The behavior prompted the assignment of those reduced current signals to the reduction of protons in the media. The block copolymer micellar solution containing P-123 (pH = 2.0) was also examined; however, no relevant differences in the electrochemical response (**Figure 1b**) were observed in relation to the solution without P-123 at a pH of 2.1. A clear reduction in current signal also began at approximately –0.50 V, although the current density was far smaller. That reduction in current density can be attributed to the adsorption of polymeric micelles on the surface of the Si/Ti/Au electrodes.

In the presence of Fe(II) and Pt(VI) species, two significant differences were observed in the response captured by CV (**Figure 1c**). The first was the appearance of a reduction peak beginning at approximately 0.30 V and thus corresponding to the reduction of platinum. Second, another reduction peak not observed in previous solutions with a maximum intensity at approximately –1.40 V, which was probably attributable to the formation of the Fe–Pt alloy.

Once the scan was redirected to the positive potentials, another oxidation peak appeared at –0.40 V, likely due to the oxidation of the Fe–Pt deposited in the cathodic scan, as suggested by the oxidation peak's increased intensity as the cathodic potential limit became increasingly negative. The superficial oxidation of the pure platinum and gold substrate was also observed at more positive potentials.

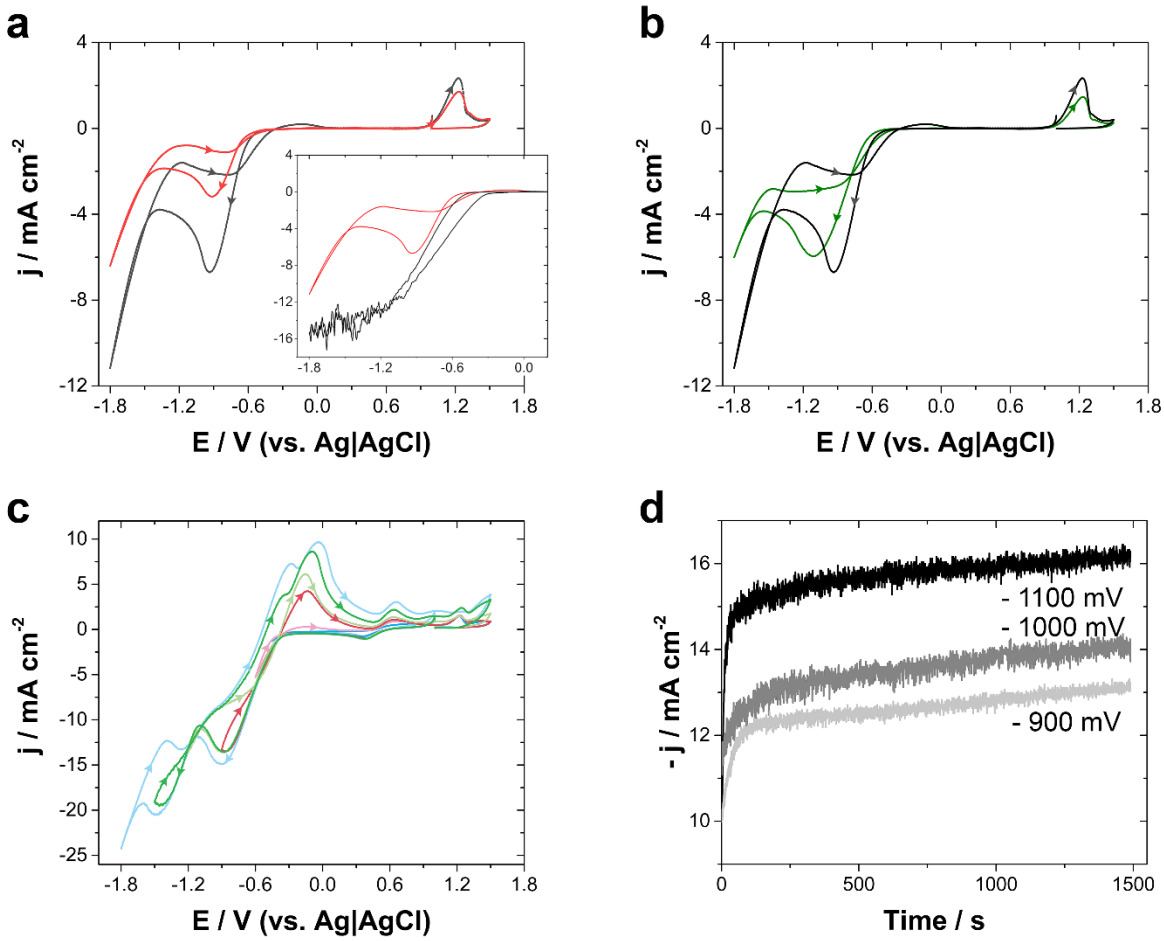

Figure 1. Cyclic voltammograms of (a) pH = 2.1 (black) and pH = 3.0 (red) blank solutions – the inset illustrates the cyclic voltammograms of the solution at pH = 2.1 in stagnant (red) and stirred (black) conditions – , (b) pH = 2.1 (black) and P-123 (pH = 2.1), and (c) Fe–Pt polymeric micellar solution (pH = 2.1) with different cathodic limits at a scan rate of 50 mV s^{-1} on the

Si/Ti/Au substrates, along with (d) chronoamperometric curves at different applied potentials at a fixed time on the Si/Ti/Au substrates.

These results recommended investigating the electrodeposition potential's effect on film integrity, mesoporous formation and definition, and the composition of Fe–Pt from –900 mV to –1,100 mV. Ultimately, more negative potentials prompted the loss of pore definition and affected the deposit's integrity as a consequence of hydrogen coevolution, whereas potentials lower than –900 mV caused the deposition of virtually pure mesoporous Pt films. A time of 1,500 s was fixed for all deposits (**Figure 1d**), independently of the potential applied. Nevertheless, the deposit's integrity, pore definition, and Fe–Pt content were practically constant at charge densities ranging from 0.5 to 12 C cm^{-2}. Although the active surface area gradually expanded as the deposition's charge density rose, the adhesion of films significantly decreased, thereby resulting in the detachment of some parts of the deposit. By contrast, at low charge densities (<0.5 C cm^{-2}), the percentage of Fe decreased, and the deposition's charge density did not exceed 12 C cm^{-2}, which adds support for the observed integrity and composition of well-defined mesoporous films. As shown in **Table 1**, the iron content on the mesoporous Fe–Pt films increased with the applied potential, as verified by EDS and ICP analysis. Moreover, as depicted in **Figure 2**, Fe–Pt deposits with excellent porosity were synthesized from –900 mV to –1,100 mV. **Table 2** additionally shows that the pore diameter increased slightly as the potential increased; even so, well-defined porosity for all samples was attained. As expected, more negative potentials significantly affected the definition of pores by increasing the iron content. The definition of a pore is known to closely relate to Pt content, because Pt (IV) species interact strongly with micelles, which themselves act as porogen agents. The specific BET surface area

of Fe–Pt films ranged from 42 to 45 $m^2 g^{-1}$ but was slightly higher at -1,000 mV, when the pore diameter and definition were greatly improved.

Potential / mV vs Ag|AgCl	**Fe / at. %**		**Pt / at. %**		**Average pore diameter / nm**	**BET surface area / $m^2 g^{-1}$**	**M_s / emu g^{-1}**	**H_c / Oe**
	EDS	**ICP-OES**	**EDS**	**ICP-OES**				
-900	19±2	18±1	81±2	82±1	~4	42	35.1	~630
-1,000	23±3	22±1	77±3	78±1	~7	48	35.2	~650
-1,100	27±2	28±1	73±2	72±1	~9	43	35.7	~690

Table 1: Deposition potential, elemental composition, pore diameter, BET surface area, saturation magnetization, coercivity of the Fe-Pt mesoporous films.

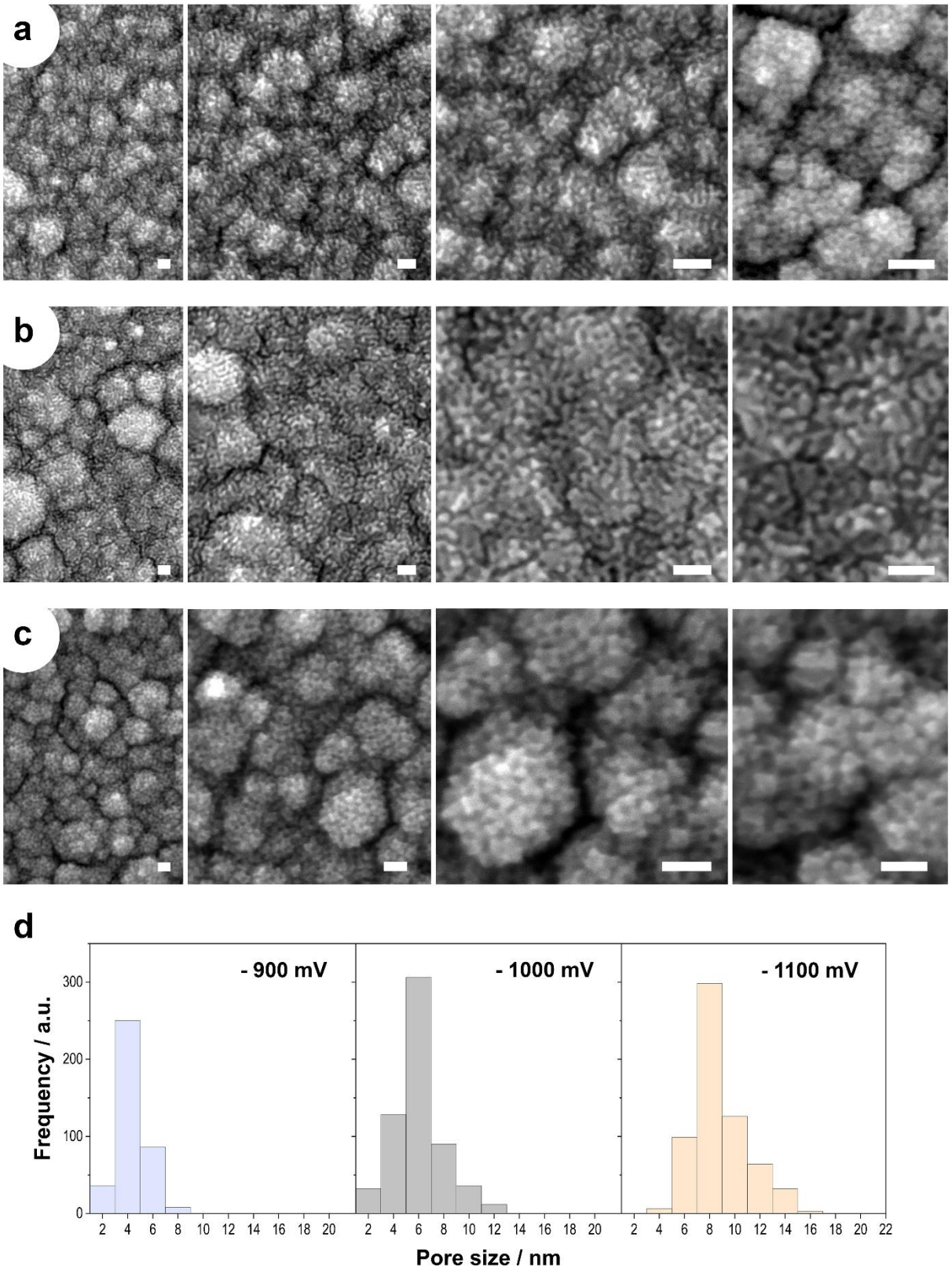
a
b
c
d
- 900 mV
- 1000 mV
- 1100 mV
Frequency / a.u.
Pore size / nm

Figure 2: FE-SEM micrographs of Fe–Pt deposits prepared at (a) –900, (b) –1,000, and (c) –1,100 mV on the Si/Ti/Au substrates. Scale bar: 40 nm. (d) Pore size histogram determined from on-top FE-SEM images.

The structure of mesoporous Fe–Pt films was examined using XRD analysis, the resulting diffraction patterns of which appear in **Figure 3a**. The strong peak observed at $2\theta = 38.1°$ was identified as the (111) diffraction of Au sputtered layer of working electrode. The principal diffraction peaks attributed to the mesoporous Fe–Pt films appeared at $2\theta = 40.3$, 46.8, 68.4, and 81.3°, which aligned neatly with the (111), (200), (220), and (311) planes, respectively, of the disordered *fcc* $Fe–Pt_3$ phase with the space group $Fm\bar{3}m$ (ICDD Ref. No. 001-089-2050) [54,55]. However, other tiny peaks, all unassigned, were also observable in all the samples. It should be noted that, regardless of composition, all deposits have the same crystal structure.

Although the magnetization curves of Fe–Pt deposits at room temperature exhibited superparamagnetic behavior, at 5 K they showed low H_c of only approximately 630–690 Oe for all of the deposits (**Figure 3b**). The amount of H_c increased with the rise in Fe content, while the M_s value of mesoporous Fe–Pt was approximately 35 emu g^{-1} [40,42,55]. Beyond that, the value of M_s increased slightly with the increase in Fe content. The magnetic properties of mesoporous Fe–Pt films were thus found to be adequate for biomedical applications.

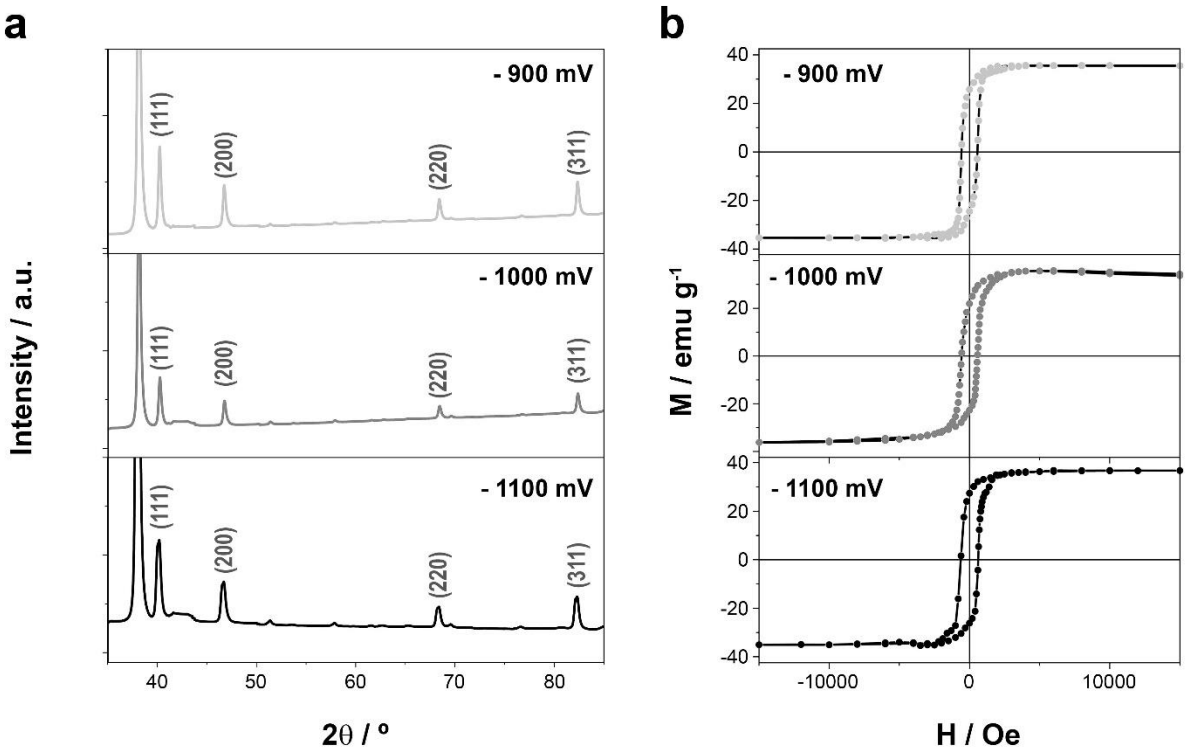

Figure 3: (a) XRD pattern and (b) magnetization curves of Fe–Pt deposits prepared at -900, -1,000, and -1,100 mV on the Si/Ti/Au substrates.

Figure 4 shows the Fe 2p and Pt 4f XPS spectra of the deposited Fe–Pt films. As shown in **Figure 4a**, two asymmetric complex bands, centered at approximately 706.7 and 719.6 eV and corresponding to Fe $2p_{3/2}$ and Fe $2p_{1/2}$ multiplet (ΔBE=12.9 eV), were clearly observable on the Fe 2p spectra. The binding energy of those two peaks was similar to the metal reference (i.e., 706.7 and 719.8 eV, Δ_{metal} = 13.1 eV), which indicates that the predominant species is Fe(0). However, the asymmetry and complexity of small bands overlapping with the respective signal of pure Fe metal indicates the presence of iron species in positive oxidation states (e.g., oxides and hydroxides). Even so, their presence was largely irrelevant, because the oxo-iron and hydroxo-iron species codeposited with Fe–Pt immediately redissolved due to the acidic media

used for electrodeposition. The deposition of Pt(0) was also confirmed by the Pt $4f_{7/2}$ and Pt $4f_{5/2}$ multiplet, centered at approximately 71.0 and 74.4 eV, respectively, which aligned perfectly with the Pt metal reference (71.0 eV, Δ_{metal} = 3.35 eV). The results of XPS confirmed the deposit of mesoporous Fe–Pt films with the minimal presence oxo–hydroxo species [40].

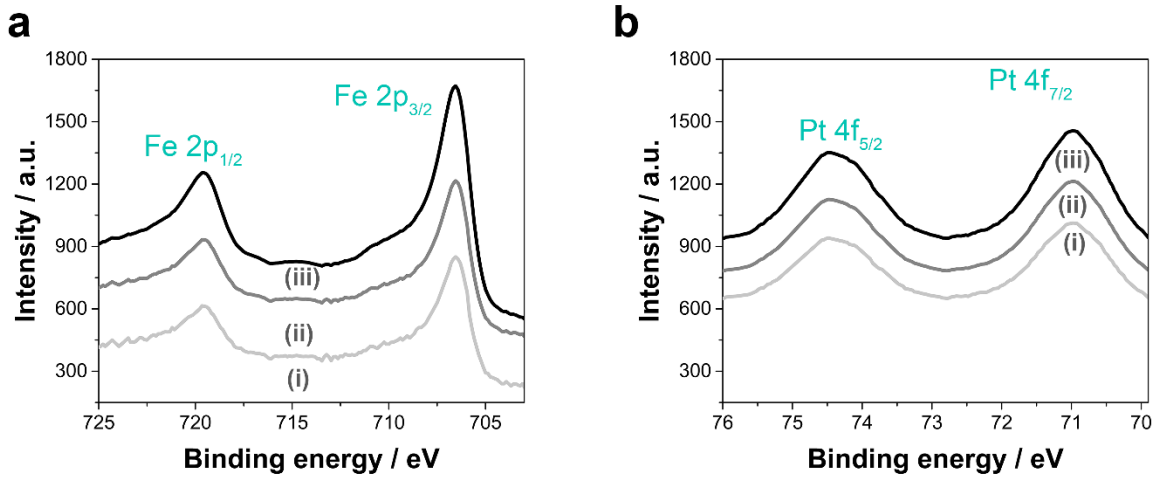

Figure 4: XPS spectra of (a) Fe 2p and (b) Pt 4f for the Fe–Pt films deposited at (i) –900, (ii) –1,000, and (iii) –1,100 mV on the Si/Ti/Au substrates.

Chemical and Electrochemical stability of Fe–Pt mesoporous films

The mesoporous nature of the deposits can lower chemical stability as a result of increased surface exposure and reactivity, which can detrimentally induce a greater release of Fe and Pt ions that could be harmful to life. For this reason, the chemical and electrochemical stability of the deposits in cell culture medium were also analyzed. First, electrochemical corrosion experiments were performed to corroborate the stability of the structures DMEM at 37 °C. **Figure 5** shows the potentiodynamic curves corresponding to the mesoporous Fe–Pt films prepared at –900, –1,000, and –1,100 mV. A positive corrosion potential between 249 and 267

mV (see **Table 2**) was observed for the different deposits, although their Fe content did not differ significantly. The corrosion potential was quite similar to that of Au films (E_{cor} = 255 mV) in the same conditions, which corroborates the excellent corrosion resistance of the mesoporous Fe–Pt prepared films. This finding is especially important, since mesoporous surfaces typically have a greater tendency to oxidize than compact films.

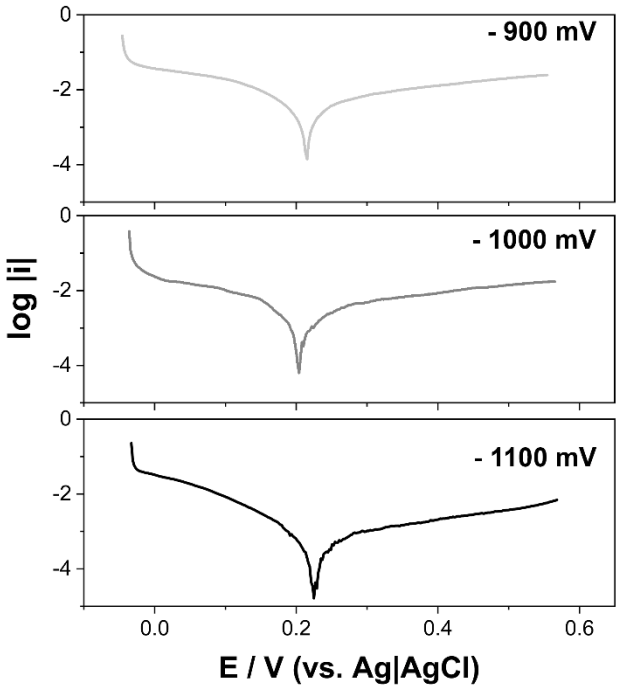

Figure 5: Potentiodynamic polarization curves in logarithmic scale corresponding to the Fe–Pt films deposited at (i) –900, (ii) –1,000, and (iii) –1,100 mV on the Si/Ti/Au substrates.

In general, the toxicity of nanostructured materials depends heavily on their dissolution and solubility in biological media. In our experiment, the chemical stability of the mesoporous Fe–Pt films in DMEM at 37 °C was investigated over a period of 160 h. **Table 2** shows the temporal evolution of the Fe and Pt concentration in the cell culture medium, as well as the percentage of

the deposit dissolved. The dissolution of Fe was slightly higher in deposits with a higher percentage of Fe, whereas the dissolution of Pt was practically identical for all the deposits. In the case of Fe, concentrations of 0.524–0.554 ppm were reached after 160 h of immersion, with 0.88–1.28% of the deposit dissolved, whereas in the case of Pt, concentrations of 0.0009–0.0011 ppm were reached after 160 h, with 0.0011–0.0019% of the deposit dissolved. The dissolution of Fe–Pt was minimal, which further justifies the material's proposed use in the manufacture of micro- and nanodevices for biomedical applications.

Potential / mV vs Ag|AgCl	**E_{cor} / mV vs Ag|AgCl**	**Time / h**	**Fe**		**Pt**		**pH**
			mg L^{-1}	**%**	**mg L^{-1}**	**%**	
-900	254	0	0.448±0.002	0.0039	n/a	n/a	7.89±0.02
		24	0.500±0.003	0.56	0.0007±0.0001	0.0009	7.80±0.03
		48	0.513±0.001	0.74	0.0009±0.0001	0.0011	7.76±0.05
		160	0.524±0.002	0.88	0.0011±0.0001	0.0019	7.71±0.02
-1,000	249	0	0.451±0.004	0.0032	n/a	n/a	7.83±0.01
		24	0.506±0.002	0.64	0.0004±0.0001	0.0005	7.86±0.02
		48	0.525±0.001	0.89	0.0006±0.0001	0.0007	7.81±0.03
		160	0.545±0.001	1.16	0.0008±0.0001	0.0010	7.78±0.04
-1,100	267	0	0.457±0.003	0.0040	n/a	n/a	7.84±0.02
		48	0.515±0.002	0.76	0.0004±0.0002	0.0006	7.80±0.04
		72	0.531±0.001	0.98	0.0007±0.0001	0.0009	7.74±0.01
		160	0.554±0.002	1.28	0.0009±0.0001	0.0011	7.70±0.02

Table 2: Corrosion potential, iron and platinum concentration, and pH of DMEM as a function of contact time at 37 °C. Values represent Means+SD (n=6)

Mechanical stability of Fe–Pt mesoporous films

To confirm the mechanical stability of Fe–Pt mesoporous films for biomedical applications, the indentation-reduced Young's modulus (E_r) and hardness (H) were measured using nanoindentation (**Figure 6**). On the one hand, E_r indicates the stiffness of a material, meaning how easily it is to bend or stretch, which the porosity of materials negatively influences. As shown in **Figure 6a**, the E_r of the Fe–Pt mesoporous films was lower than the maximum value

reported for bulk solid films of Fe (E_r = 212 GPa) but similar or even slightly greater than the maximum value reported for bulk solid films of Pt (E_r = 172 GPa), regardless of the porosity of the thin films. In our deposits, the increase in Fe also implies an increase in pore size, from 4 nm at –900 mV to 9 nm at –1,100 mV, which could translate into a reduced Young's modulus. Although porosity's effect could not be determined, the increase in Fe on Fe–Pt mesoporous films slightly increased the E_r values. However, the increase could be more important in the case of compact materials. On the other hand, hardness indicates a material's resistance to scratching. The Fe–Pt mesoporous films exhibited hardness values from 5 to 6.5 GPa, which were higher than ones reported for the bulk solid films of Fe or Pt (**Figure 6b**). Those high values can be attributed to the nanocrystallinity or internal stresses of the Fe–Pt mesoporous film matrix[56]. Beyond that, the hardness of the Fe–Pt mesoporous films increased as the Fe content increased. Taken together, the reduced Young's modulus (E_r) and hardness (H) of the Fe–Pt mesoporous films suggests the promising use of the films in biomedical applications.

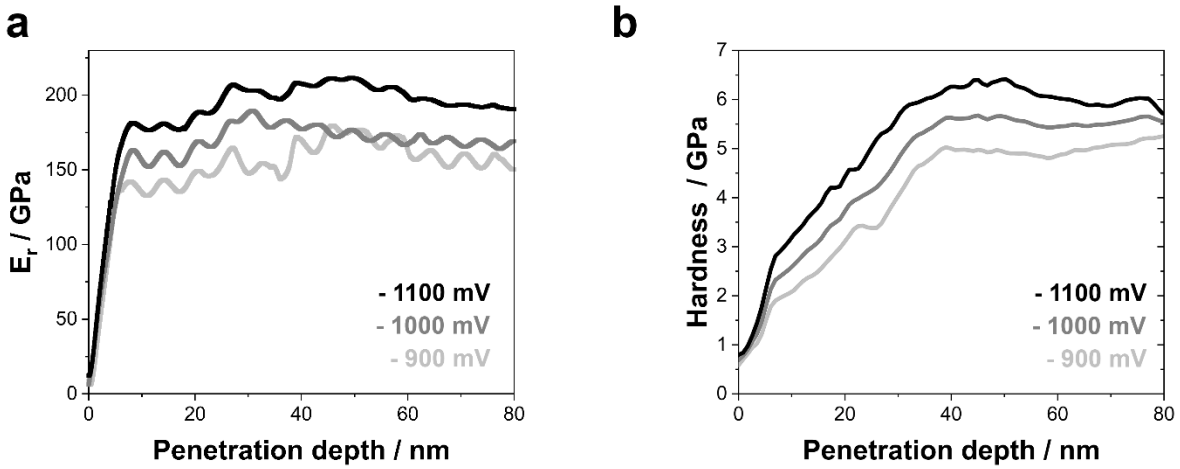

Figure 6: Representative curves of (a) the reduced Young's modulus (E_r) and (b) hardness (H) as a function of the penetration depth of Fe–Pt mesoporous films with nanoindentation.

Cytotoxicity of Fe–Pt mesoporous films

The biocompatibility of the mesoporous Fe-Pt films was confirmed by assessing the cell viability of HaCaT keratinocytes in presence of the material. HaCaT cells were chosen for being widely used to study the biocompatibility of different materials,[49–52] due to its high capacity to proliferate and differentiate in vitro.[57] For this, cells were incubated for 48 h in presence of Si/Ti/Au substrates with Fe-Pt films deposited at –900,–1,000, and–1,100 mV. Cell viability respect to cells incubated without the presence of substrates (untreated) was assessed by means of MTT assays which determines the mitochondrial enzymatic activity (see Supporting Information, **Table S1**).

Figure 7 shows that the incubation of HaCaT cells in presence of the Si/Ti/Au substrates with or without Fe-Pt films does not decrease cell viability, which relates well with the chemical stability of the material in biological media. Nonetheless, it is interesting that the presence of Fe-Pt films induces a slight increase in viability values, especially those deposited at -1,000 mV (117.2 ± 3.6 % cell viability). Although no significant differences were observed respect to untreated cells ($P>0.05$) according to statistical analyses (see Supporting Information, **Table S2**), such slight increase could probably be related to the rugosity of the mesoporous material as observed by SEM (**Figure 2**), and its overall increased surface area as compared to tight films (Si/Ti/Au), which could facilitate the adhesion and growth of a larger number of cells on the surface of the material. These results confirm the biocompatibility of Fe-Pt films, making them suitable for biomedical applications.

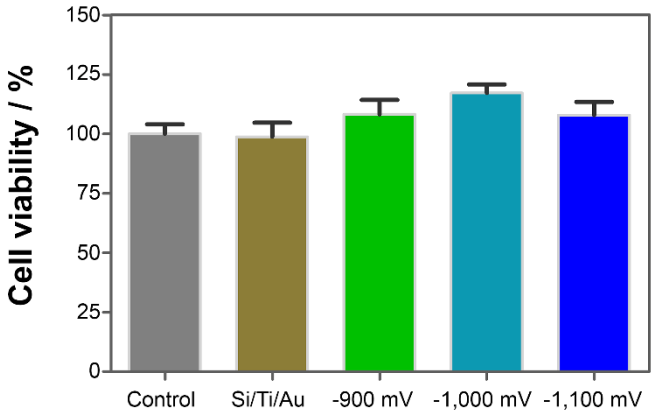

Figure 7: Cell viability of HaCaT keratinocytes after 48-h incubation in presence of Si/Ti/Au substrates containing Fe-Pt films deposited at -900, -1,000, and -1,100 mV, or substrates without Fe-Pt. Cells grown in culture medium were taken as control. Values represent Means±SD (n=3). No significant differences between groups were observed ($P>0.05$).

Conclusions

Well-defined mesoporous Fe-Pt films with tunable elemental composition and pore size have been successfully electrodeposited using a simple triblock copolymer micellar solution as electrochemical media on Si/Ti/Au substrates. By using this process, films with hemispherical-like grain morphology with a well-distributed uniform porosity (pore sizes ranged from 5 to 9 nm, depending on the applied potential, being larger when the potential was more negative) were obtained, offering high accessible surface areas (ranged from 42 to 48 m^2g^{-1}). The preparation strategy is potentially extensible to other substrates and could be combined with hard templates to electrosynthesize more complex architectures like nanowires, nanorods, and micro helices.

The prepared mesoporous Fe-Pt films exhibit excellent corrosion resistance, comparable to pure Pt and Au, in biological media at 37ºC. Also, the mesoporous Fe-Pt films pose high chemical stability, with minimal release of Fe and Pt ions, after 160 h of immersion in biological media at 37ºC (~0.88 % of Fe and ~0.0019 % of Pt) and mechanical stability (i.e., E_r ranged from 150 to 200 GPa and H ranged from 5 to 6.5 GPa). These findings are very relevant to demonstrate this material's robustness as a candidate to manufacture in the future micro/nano biomedical platforms. The release and dissolution of metal nanostructures are some of the main limitations of the cytotoxicity of materials. A proof of concept has been carried out to verify the harmless effect of the prepared material on the living cell, a crucial aspect for the viability of the material's use. Importantly, these materials' extremely low cytotoxicity is proved by incubating them with HaCaT cells (human immortalized keratinocytes). It is important to note that the mesoporous Fe-Pt material has no negative effects on cell viability. Consequently, Fe-Pt mesoporous films are suitable candidates for biomedical applications.

ASSOCIATED CONTENT

Supporting Information.

The following files are available free of charge.

Cytotoxicity of Fe–Pt mesoporous films

AUTHOR INFORMATION

Corresponding Author

Dr. Albert Serrà (a.serra@ub.edu) ORCID 0000-0003-0147-3400

Prof. Elvira Gómez (e.gomez@ub.edu) ORCID 0000-0002-9223-6357

Author Contributions

The manuscript was written through contributions of all authors. All authors have given approval to the final version of the manuscript.

Funding Sources

This work was supported by TEC2017-85059-C3-2-R project (financed by the Fondo Europeo de Desarrollo Regional, FEDER) from the Spanish *Ministerio de Economía y Competitividad* (MINECO).

Notes

ACKNOWLEDGEMENTS

The authors thank the CCiTUB for the use of their equipment. Prof. Laura Baldomà and Prof. Josefa Badia from the Biochemistry and Physiology Department at the Faculty of Pharmacy and Food Science of the Universitat de Barcelona are acknowledged for their kind support with viability studies.

REFERENCES

(1) Cheng, L.; Wang, C.; Feng, L.; Yang, K.; Liu, Z. Functional Nanomaterials for Phototherapies of Cancer. *Chem. Rev.* **2014**, *114* (21), 10869–10939. https://doi.org/10.1021/cr400532z.

(2) Fan, W.; Yung, B.; Huang, P.; Chen, X. Nanotechnology for Multimodal Synergistic Cancer Therapy. *Chem. Rev.* **2017**, *117* (22), 13566–13638. https://doi.org/10.1021/acs.chemrev.7b00258.

(3) Yin, P. T.; Shah, S.; Chhowalla, M.; Lee, K. B. Design, Synthesis, and Characterization of Graphene-Nanoparticle Hybrid Materials for Bioapplications. *Chem. Rev.* **2015**, *115* (7), 2483–2531. https://doi.org/10.1021/cr500537t.

(4) El-Toni, A. M.; Habila, M. A.; Labis, J. P.; Alothman, Z. A.; Alhoshan, M.; Elzatahry, A. A.; Zhang, F. Design, Synthesis and Applications of Core-Shell, Hollow Core, and Nanorattle Multifunctional Nanostructures. *Nanoscale* **2016**, *8* (5), 2510–2531. https://doi.org/10.1039/c5nr07004j.

(5) Mohapatra, S.; Rout, S. R.; Das, R. K.; Nayak, S.; Ghosh, S. K. Highly Hydrophilic Luminescent Magnetic Mesoporous Carbon Nanospheres for Controlled Release of Anticancer Drug and Multimodal Imaging. *Langmuir* **2016**, *32* (6), 1611–1620. https://doi.org/10.1021/acs.langmuir.5b03898.

(6) Serrà, A.; Gimeno, N.; Gómez, E.; Mora, M.; Sagristá, M. L.; Vallés, E. Magnetic Mesoporous Nanocarriers for Drug Delivery with Improved Therapeutic Efficacy. *Adv. Funct. Mater.* **2016**, *26* (36), 6601–6611. https://doi.org/10.1002/adfm.201601473.

(7) Serrà, A.; Vallés, E.; García-Torres, J. Electrochemically Synthesized Nanostructures for the Manipulation of Cells: Biohybrid Micromotors. *Electrochem. commun.* **2017**, *85* (October), 27–31. https://doi.org/10.1016/j.elecom.2017.11.002.

(8) Katz, E.; Willner, I. Integrated Nanoparticle-Biomolecule Hybrid Systems: Synthesis, Properties, and Applications. *Angew. Chemie - Int. Ed.* **2004**, *43* (45), 6042–6108. https://doi.org/10.1002/anie.200400651.

(9) Sapsford, K. E.; Algar, W. R.; Berti, L.; Gemmill, K. B.; Casey, B. J.; Oh, E.; Stewart, M. H.; Medintz, I. L. Functionalizing Nanoparticles with Biological Molecules: Developing Chemistries That Facilitate Nanotechnology. *Chem. Rev.* **2013**, *113* (3), 1904–2074. https://doi.org/10.1021/cr300143v.

(10) Wege, C.; Koch, C. From Stars to Stripes: RNA-Directed Shaping of Plant Viral Protein Templates—Structural Synthetic Virology for Smart Biohybrid Nanostructures. *Wiley Interdiscip. Rev. Nanomedicine Nanobiotechnology* **2020**, *12* (2), 1–44. https://doi.org/10.1002/wnan.1591.

(11) Serrà, A.; García-Torres, J. Electrochemistry: A Basic and Powerful Tool for Micro- and Nanomotor Fabrication and Characterization. *Appl. Mater. Today* **2021**, *22*. https://doi.org/10.1016/j.apmt.2021.100939.

(12) Chen, C.; Karshalev, E.; Guan, J.; Wang, J. Magnesium-Based Micromotors: Water-Powered Propulsion, Multifunctionality, and Biomedical and Environmental Applications. *Small* **2018**, *14* (23), 1–10. https://doi.org/10.1002/smll.201704252.

(13) Singh, V. V.; Kaufmann, K.; de Ávila, B. E. F.; Karshalev, E.; Wang, J. Molybdenum Disulfide-Based Tubular Microengines: Toward Biomedical Applications. *Adv. Funct. Mater.* **2016**, *26* (34), 6270–6278. https://doi.org/10.1002/adfm.201602005.

(14) Serrà, A.; Vázquez-Mariño, G.; García-Torres, J.; Bosch, M.; Vallés, E. Magnetic Actuation of Multifunctional Nanorobotic Platforms to Induce Cancer Cell Death. *Adv. Biosyst.* **2018**, *1700220*, 1700220. https://doi.org/10.1002/adbi.201700220.

(15) Safdar, M.; Khan, S. U.; Jänis, J. Progress toward Catalytic Micro- and Nanomotors for Biomedical and Environmental Applications. *Adv. Mater.* **2018**, *30* (24), 1–27. https://doi.org/10.1002/adma.201703660.

(16) Qiu, M.; Ren, W. X.; Jeong, T.; Won, M.; Park, G. Y.; Sang, D. K.; Liu, L. P.; Zhang, H.; Kim, J. S. Omnipotent Phosphorene: A next-Generation, Two-Dimensional Nanoplatform for Multidisciplinary Biomedical Applications. *Chem. Soc. Rev.* **2018**, *47* (15), 5588–5601. https://doi.org/10.1039/c8cs00342d.

(17) Alea-Reyes, M. E.; Rodrigues, M.; Serrà, A.; Mora, M.; Sagristá, M. L.; González, A.; Durán, S.; Duch, M.; Plaza, J. A.; Vallés, E.; Russell, D. A.; Pérez-García, L. Nanostructured Materials for Photodynamic Therapy: Synthesis, Characterization and in Vitro Activity. *RSC Adv.* **2017**, *7* (28), 16963–16976. https://doi.org/10.1039/c7ra01569k.

(18) Yong S.Cho, H. D. G. and V. R. W. A. *Encyclopedia of Nanoscience and Nanotechnology*; 2004; Vol. 1. https://doi.org/10.1081/E-ENN.

(19) Xia, X.; Tu, J.; Zhang, Y.; Chen, J.; Wang, X.; Gu, C.; Guan, C.; Luo, J.; Fan, H. J. Porous Hydroxide Nanosheets on Preformed Nanowires by Electrodeposition: Branched Nanoarrays for Electrochemical Energy Storage. *Chem. Mater.* **2012**, *24* (19), 3793–3799. https://doi.org/10.1021/cm302416d.

(20) Serrà, A.; Vallés, E. Advanced Electrochemical Synthesis of Multicomponent Metallic Nanorods and Nanowires: Fundamentals and Applications. *Appl. Mater. Today* **2018**, *12*, 207–234. https://doi.org/10.1016/j.apmt.2018.05.006.

(21) Kicir, N.; Tüken, T.; Erken, O.; Gumus, C.; Ufuktepe, Y. Nanostructured ZnO Films in Forms of Rod, Plate and Flower: Electrodeposition Mechanisms and Characterization. *Appl. Surf. Sci.* **2016**, *377* (3), 191–199. https://doi.org/10.1016/j.apsusc.2016.03.111.

(22) Ramachandramoorthy, R.; Mieszala, M.; Manzano, C. V.; Maeder, X.; Michler, J.; Philippe, L. Dual-Templated Electrodeposition and Characterization of Regular Metallic Foam Based Microarchitectures. *Appl. Mater. Today* **2020**, *20*, 100667. https://doi.org/10.1016/j.apmt.2020.100667.

(23) Frantz, C.; Vichery, C.; Zechner, J.; Frey, D.; Bürki, G.; Cebeci, H.; Michler, J.; Philippe, L. Pulse Electrodeposition of Adherent Nickel Coatings onto Anodized Aluminium Surfaces. *Appl. Surf. Sci.* **2015**, *330*, 39–47. https://doi.org/10.1016/j.apsusc.2014.12.091.

(24) Albanese, A.; Tang, P. S.; Chan, W. C. W. The Effect of Nanoparticle Size, Shape, and Surface Chemistry on Biological Systems. *Annu. Rev. Biomed. Eng.* **2012**, *14*, 1–16. https://doi.org/10.1146/annurev-bioeng-071811-150124.

(25) Kumar, C. S. S. R.; Mohammad, F. Magnetic Nanomaterials for Hyperthermia-Based Therapy and Controlled Drug Delivery. *Adv. Drug Deliv. Rev.* **2011**, *63* (9), 789–808. https://doi.org/10.1016/j.addr.2011.03.008.

(26) De Ávila, B. E. F.; Angsantikul, P.; Li, J.; Angel Lopez-Ramirez, M.; Ramírez-Herrera, D. E.; Thamphiwatana, S.; Chen, C.; Delezuk, J.; Samakapiruk, R.; Ramez, V.; Zhang, L.; Wang, J. Micromotor-Enabled Active Drug Delivery for in Vivo Treatment of Stomach Infection. *Nat. Commun.* **2017**, *8* (1), 1–8. https://doi.org/10.1038/s41467-017-00309-w.

(27) Seehra, M. S.; Singh, V.; Dutta, P.; Neeleshwar, S.; Chen, Y. Y.; Chen, C. L.; Chou, S. W.; Chen, C. C. Size-Dependent Magnetic Parameters of Fcc FePt Nanoparticles: Applications to Magnetic Hyperthermia. *J. Phys. D. Appl. Phys.* **2010**, *43* (14). https://doi.org/10.1088/0022-3727/43/14/145002.

(28) Mohammadi Ziarani, G.; Malmir, M.; Lashgari, N.; Badiei, A. The Role of Hollow Magnetic Nanoparticles in Drug Delivery. *RSC Adv.* **2019**, *9* (43), 25094–25106. https://doi.org/10.1039/c9ra01589b.

(29) Luo, H.; Sun, L.; Lu, Y.; Yan, Y. Electrodeposition of Mesoporous Semimetal and Magnetic Metal Films from Lyotropic Liquid Crystalline Phases. *Langmuir* **2004**, *20* (23), 10218–10222. https://doi.org/10.1021/la036367.

(30) Serrà, A.; Vallés, E. Microemulsion-Based One-Step Electrochemical Fabrication of Mesoporous Catalysts. *Catalysts* **2018**, *8* (9), 1–22. https://doi.org/10.3390/catal8090395.

(31) Nugraha, A. S.; Na, J.; Hossain, M. S. A.; Lin, J.; Kaneti, Y. V.; Iqbal, M.; Jiang, B.; Bando, Y.; Asahi, T.; Yamauchi, Y. Block Copolymer-Templated Electrodeposition of Mesoporous Au-Ni Alloy Films with Tunable Composition. *Appl. Mater. Today* **2020**, *18*, 100526. https://doi.org/10.1016/j.apmt.2019.100526.

(32) Sugih Nugraha, A.; Malgras, V.; Iqbal, M.; Jiang, B.; Li, C.; Bando, Y.; Alshehri, A.; Kim, J.; Yamauchi, Y.; Asahi, T. Electrochemical Synthesis of Mesoporous Au−Cu Alloy Films with Vertically Oriented Mesochannels Using Block Copolymer Micelles. *ACS Appl. Mater. Interfaces* **2018**, *10*, 28. https://doi.org/10.1021/acsami.8b05517.

(33) Li, C.; Malgras, V.; Alshehri, S. M.; Kim, J. H.; Yamauchi, Y. Electrochemical Synthesis of Mesoporous Pt Nanowires with Highly Electrocatalytic Activity toward Methanol Oxidation Reaction. *Electrochim. Acta* **2015**, *183*, 107–111. https://doi.org/10.1016/j.electacta.2015.04.028.

(34) Cardoso, M. B.; Da Cruz Schneid, A.; Silveira, C. P.; Galdino, F. E.; Ferreira, L. F.; Bouchmella, K. Colloidal Stability and Redispersibility of Mesoporous Silica Nanoparticles in Biological Media. *Langmuir* **2020**, *36* (39), 11442–11449. https://doi.org/10.1021/acs.langmuir.0c01571.

(35) Serra, A.; Artal, R.; Philippe, L.; Elvira, G. Electrodeposited Ni-Rich Ni − Pt Mesoporous Nanowires for Selective and Efficient Formic Acid-Assisted Hydrogenation of Levulinic Acid to γ - Valerolactone. *Langmuir* **2021**, *37 (15)*, 4666–4677 https://doi.org/10.1021/acs.langmuir.1c00461.

(36) Isarain-Chávez, E.; Baró, M. D.; Alcantara, C.; Pané, S.; Sort, J.; Pellicer, E. Micelle-Assisted Electrodeposition of Mesoporous Fe–Pt Smooth Thin Films and Their Electrocatalytic Activity towards the Hydrogen Evolution Reaction. *ChemSusChem* **2018**, *11* (2), 367–375. https://doi.org/10.1002/cssc.201701938.

(37) Artal, R.; Serr, A.; Michler, J.; Philippe, L.; Elvira, G. Electrodeposition of Mesoporous Ni-Rich Ni-Pt Films for Highly Efficient Methanol Oxidation. *Nanomaterials* **2020**, *10 (8)*, 1–17, 1435. https://doi.org/10.3390/nano10081435.

(38) Navarro-Senent, C.; Pané, S.; Sort, J.; Pellicer, E. The Order of Addition and Time Matters: Impact of Electrolyte Processing on Micelle-Assisted Electrosynthesis of Mesoporous Alloys. *Electrochim. Acta* **2020**, *358*. https://doi.org/10.1016/j.electacta.2020.136940.

(39) Zhang, J.; Quintana, A.; Menéndez, E.; Coll, M.; Pellicer, E.; Sort, J. Electrodeposited Ni-Based Magnetic Mesoporous Films as Smart Surfaces for Atomic Layer Deposition: An "All-Chemical" Deposition Approach toward 3D Nanoengineered Composite Layers. *ACS*

Appl. Mater. Interfaces **2018**, *10* (17), 14877–14885. https://doi.org/10.1021/acsami.8b01626.

(40) Isarain-Chávez, E.; Baró, M. D.; Alcantara, C.; Pané, S.; Sort, J.; Pellicer, E. Micelle-Assisted Electrodeposition of Mesoporous Fe–Pt Smooth Thin Films and Their Electrocatalytic Activity towards the Hydrogen Evolution Reaction. *ChemSusChem* **2018**, *11* (2), 367–375. https://doi.org/10.1002/cssc.201701938.

(41) Sun, S. Recent Advances in Chemical Synthesis, Self-Assembly, and Applications of FePt Nanoparticles. *Adv. Mater.* **2006**, *18* (4), 393–403. https://doi.org/10.1002/adma.200501464.

(42) Kadiri, V. M.; Bussi, C.; Holle, A. W.; Son, K.; Kwon, H.; Schütz, G.; Gutierrez, M. G.; Fischer, P. Biocompatible Magnetic Micro- and Nanodevices: Fabrication of FePt Nanopropellers and Cell Transfection. *Adv. Mater.* **2020**, *32* (25). https://doi.org/10.1002/adma.202001114.

(43) Chou, S. W.; Shau, Y. H.; Wu, P. C.; Yang, Y. S.; Shieh, D. Bin; Chen, C. C. In Vitro and in Vivo Studies of Fept Nanoparticles for Dual Modal CT/MRI Molecular Imaging. *J. Am. Chem. Soc.* **2010**, *132* (38), 13270–13278. https://doi.org/10.1021/ja1035013.

(44) Kitamoto, Y.; He, J. S. Chemical Synthesis of FePt Nanoparticles with High Alternate Current Magnetic Susceptibility for Biomedical Applications. *Electrochim. Acta* **2009**, *54* (25), 5969–5972. https://doi.org/10.1016/j.electacta.2009.02.092.

(45) Shi, Y.; Lin, M.; Jiang, X.; Liang, S. Recent Advances in FePt Nanoparticles for Biomedicine. *J. Nanomater.* **2015**, *2015*. https://doi.org/10.1155/2015/467873.

(46) Goswami, M. M.; Das, A.; De, D. Wetchemical Synthesis of FePt Nanoparticles: Tuning of Magnetic Properties and Biofunctionalization for Hyperthermia Therapy. *J. Magn. Magn. Mater.* **2019**, *475* (October 2018), 93–97. https://doi.org/10.1016/j.jmmm.2018.11.024.

(47) Kang, Z.; Peng, Y.; Zhou, L.; Li, Z.; Wang, T.; Zhang, Z.; Liao, Q.; Gao, J.; Li, Y.; Zhang, Y. Thermo-Responsive Phase-Transition Polymer Grafted Magnetic FePt Nanoparticles with Tunable Critical Temperature for Controlled Drug Release. *Mater. Chem. Front.* **2018**, *2* (9), 1609–1617. https://doi.org/10.1039/c8qm00154e.

(48) Fuchigami, T.; Kawamura, R.; Kitamoto, Y.; Nakagawa, M.; Namiki, Y. A Magnetically Guided Anti-Cancer Drug Delivery System Using Porous FePt Capsules. *Biomaterials* **2012**, *33* (5), 1682–1687. https://doi.org/10.1016/j.biomaterials.2011.11.016.

(49) Schoop, V. M.; Mirancea, N.; Fusenig, N. E. Epidermal Organization and Differentiation of HaCat Keratinocytes in Organotypic Coculture with Human Dermal Fibroblasts. *J. Invest. Dermatol.* **1999**, *112* (3), 343–353. https://doi.org/10.1046/j.1523-1747.1999.00524.x.

(50) Wiegand, C.; Hipler, U. C. Evaluation of Biocompatibility and Cytotoxicity Using Keratinocyte and Fibroblast Cultures. *Skin Pharmacol. Physiol.* **2009**, *22* (2), 74–82. https://doi.org/10.1159/000178866.

(51) Coletti, C.; Jaroszeski, M. J.; Pallaoro, A.; Hoff, A. M.; Iannotta, S.; Saddow, S. E. Biocompatibility and Wettability of Crystalline SiC and Si Surfaces. *Annu. Int. Conf. IEEE*

Eng. Med. Biol. - Proc. **2007**, No. Di, 5849–5852. https://doi.org/10.1109/IEMBS.2007.4353678.

(52) Yslas, E. I.; Cavallo, P.; Acevedo, D. F.; Barbero, C. A.; Rivarola, V. A. Cysteine Modified Polyaniline Films Improve Biocompatibility for Two Cell Lines. *Mater. Sci. Eng. C* **2015**, *51*, 51–56. https://doi.org/10.1016/j.msec.2015.02.049.

(53) Oliver, W. C.; Pharr, G. M. An Improved Technique for Determining Hardness and Elastic Modulus Using Load and Displacement Sensing Indentation Experiments. *J. Mater. Res.* **1992**, *7* (6), 1564–1583. https://doi.org/10.1557/JMR.1992.1564.

(54) Sarmphim, P.; Soontaranon, S.; Sirisathitkul, C.; Harding, P.; Kijamnajsuk, S.; Chayasombat, B.; Pinitsoontorn, S.; Chingunpitak, J. FePt3 Nanosuspension Synthesized from Different Precursors - A Morphological Comparison by SAXS, DLS and TEM. *Bull. Polish Acad. Sci. Tech. Sci.* **2017**, *65* (1), 79–84. https://doi.org/10.1515/bpasts-2017-0010.

(55) Akbulut, M. K.; Harreiß, C.; Löffler, M.; Mayrhofer, K. J. J.; Schöbitz, M.; Bachmann, J.; Spiecker, E.; Hock, R.; Kryschi, C. Facile One-Pot Synthesis of Water-Soluble Fcc FePt3 Alloy Nanostructures. *SN Appl. Sci.* **2020**, *2* (10), 1–8. https://doi.org/10.1007/s42452-020-03544-x.

(56) Eiler, K.; Fornell, J.; Navarro-Senent, C.; Pellicer, E.; Sort, J. Tailoring Magnetic and Mechanical Properties of Mesoporous Single-Phase Ni-Pt Films by Electrodeposition. *Nanoscale* **2020**, *12* (14), 7749–7758. https://doi.org/10.1039/c9nr10757f.

(57) Schurer, N.; Kohne, A.; Schliep, V.; Barlag, K.; Goerz, G. Lipid Composition and Synthesis of HaCaT Cells, an Immortalized Human Keratinocyte Line, in Comparison with Normal Human Adult Keratinocytes. *Exp. Dermatol.* **1993**, *2* (4), 179–185. https://doi.org/10.1111/j.1600-0625.1993.tb00030.x.